JOURNAL OF PROPULSION AND POWER
Vol. 10, No. 6, Nov.–Dec. 1994

Optimization of Heat Transfer in a High-Energy Booster Rocket

Christopher Tarpley* and Mark J. Lewis†
University of Maryland, College Park, Maryland 20742

This article describes the performance optimization of a high-energy booster rocket powered by the proton/antiproton annihilation reaction. This procedure can be used to evaluate and optimize new concepts for advanced high-energy propulsion systems as well as to improve performance in nuclear thermal engines if coupled with a neutronics code. The analysis includes a one-speed estimation of the gamma radiation transport in the engine shield and an analysis of the heat transfer to the hydrogen working fluid as it flows through the engine. The engine performance model is optimized using the method of feasible directions concept as implemented in the CONMIN Fortran package. CONMIN is used to explore the performance limit of this conceptual design and develop sensitivity information from which conclusions are drawn about the direction of future work. The optimized engine has a specific impulse of 1037 s. The total launch system mass as designed is 890,000 kg, which includes a payload of 50,000 kg.

Nomenclature

f	=	objective function
g	=	vector of constraints
$g_1, \ldots$	=	components of the vector of constraints
I_{sp}	=	specific impulse in s
k	=	tube packing factor
$\dot{m}$	=	fluid flow in kg s^{-1}
T	=	temperature in K
X	=	vector of design variables
$X_1, \ldots$	=	components of the vector of design variables
ΔP	=	pressure change in N/m^2

Introduction

THIS work is motivated by our interest in the application of optimization principles to discover the performance limit of the conceptual designs of a high-energy booster rocket. The type of engine used as a test case is the antimatter-powered rocket engine.

The idea of using antimatter in a rocket engine was first proposed by Sänger[1] in 1953. He wanted to use the photons from the annihilation of an electron and a positron to power the spacecraft. Forward was responsible for reviving interest in the topic and produced a study for the Air Force in 1985[2] that is the primer for antimatter propulsion. In Italy, Vulpetti[3] is leading a research effort into the use of solid core (similar to nuclear engine designs) antimatter rocket engines. In the U.S., research has been conducted by several authors. They have analyzed interplanetary missions,[4] interstellar missions,[5] and a Mars mission.[6] LaPointe[7] analyzed the use of antiprotons in a pulsed plasma engine. In all but the interstellar missions, the mixing ratio of antimatter to matter is very small. Howe[6] estimated that only 100 mg of antimatter would be required to heat the 3.4×10^5 kg of hydrogen needed for a round-trip mission to Mars.

The feasibility of antimatter propulsion will depend on having the technology for the manufacture and handling of antimatter in place. This is by no means a trivial assumption. If existing facilities were dedicated to the production of antimatter, we could produce on the order of 10^{13} antiprotons/yr,[8] with energy conversion efficiencies[2] on the order of 10^{-9}. These numbers are based on data from high-energy physics laboratories where antiprotons are routinely manufactured in accelerators for use in high-energy physics experiments. Gabrielse at Harvard is pursuing the technology for handling and storing antiprotons outside of accelerators. He has constructed[9] an antiproton trap and held 10^5 antiprotons for at least 24 h.

Forward has estimated[2] that antiproton production efficiencies can be increased by 4 to 5 orders of magnitude with current knowledge of the processes involved. He has estimated that antiprotons could be produced for \$10M/mg. This requires dedicated power sources and accelerators that imply significant capital investment. Space propulsion applications may support this kind of investment in the future.

In addition to their use in particle physics experiments, antiprotons can be used in medical and imaging technologies. Applications in these areas have been shown for antiproton quantities on the order of 10^{11}. With this technology, better image resolution with a lower radiation dose to the patient is possible. Applications in non-destructive testing (NDT) technology are also foreseen. It is hoped that these applications will drive the development of antimatter technology to the point that development of rocket engines is feasible.

Engine Design

The primary design constraint for this booster rocket engine[10] is the requirement for a shielded annihilation region. This prevents the high-energy radiation produced during operation from harming the crew, payload, or the public, and induced radioactivity from harming service personnel between flights. Operational procedures and flight paths can decrease the danger from crash scenarios.

This engine has a cylindrical combustion chamber shielded by tungsten walls, and a plug nozzle designed to prevent line-of-sight radiation from escaping through the throat. The engine is aligned with its cylindrical axis along the long axis of the rocket. The combustion chamber walls are made of several layers that are regeneratively cooled by the hydrogen working fluid. Cold hydrogen starts at the aft end of the engine, passes forward through the chamber walls, and is heated while providing a heat sink for the heat from the gamma radiation released by the annihilation reaction. The fluid then passes

Presented as Paper 92-4689 at the AIAA/SAE/ASME/ASEE 28th Joint Propulsion Conference and Exhibit, Nashville, TN, July 6–8, 1992; received Aug. 10, 1992; revision received April 2, 1994; accepted for publication April 2, 1994.

*Graduate Research Assistant, Department of Aerospace Engineering. Member AIAA.

†Assistant Professor, Department of Aerospace Engineering. Member AIAA.

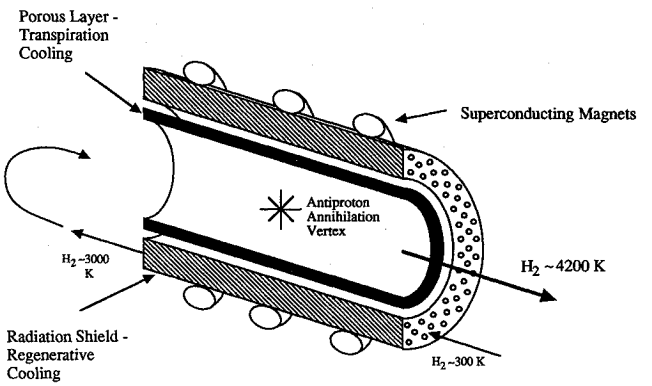

Fig. 1 Tungsten shell engine concept. Magnets on either end of the engine are not shown.

back down the hollow core of the engine and is heated further by the charged particles from the annihilation reaction as shown in Fig. 1. The hot hydrogen is then expanded with a plug nozzle to provide thrust.

The higher hydrogen temperature achieved by this design requires that sufficient cooling be applied at the inner chamber wall and to the plug to maintain their surface temperatures below the melting point of the material. The proposed design for this engine will include an inner porous layer, followed by a fluid channel for the transpiration coolant, and then the tungsten shield. A layer of low-density insulation between the tungsten shield and the coolant channel will also be included in the design. This will prevent high heating of the coolant by contact with tungsten with its enormous stopping power for radiation and high thermal conductivity. The hydrogen passes through tubes in the chamber walls as well as through an annular channel behind the porous layer. Zirconium oxide ZrO_2 will be used for both the porous layer and the insulating layer. It has a melting point of 2900 K and a maximum use temperature of 2700 K. Tubes through the tungsten and insulation will regeneratively cool these layers. It will be assumed that the porous layer can be manufactured with whatever porosity is necessary to pass the mass flow required to maintain its surface temperature below 2700 K. Although not included in this analysis, the plug nozzle would be protected by a similar mechanism.

A preliminary performance estimate to size the system has been done[11] given the requirement for total shielding of the annihilation area and the thrust requirement for liftoff. It was estimated that an I_{sp} of 1630 s could be achieved. Table 1 is a summary of the nominal design parameters for this rocket engine and Fig. 2 shows the details of the engine shield structural design.

Antimatter technology is a fascinating subject in which much work remains to be done. One antimatter containment method proposes[2] electrostatically levitating small (like salt crystals in a salt shaker) crystals of frozen antihydrogen in a vacuum. It is postulated that small amounts of antimatter can be driven off the crystals by properly tuned lasers and guided from the containment area to the combustion area. By controlling the power in the lasers, the amount of antimatter injected into the engine could be controlled in order to provide a throttling mechanism.

A preliminary analysis of the stresses produced in the shield by thermal expansion was done,[12] but is not included here. As expected, there are large compressive stresses in the inner layer and the outer layer is in tension. In the inner layer, compression could lead to the closing of tubes and the development of hot spots. The problems associated with these stresses are formidable and would provide fertile ground for future work.

Engine Performance Analysis

The structure is divided into 100 axial segments running from the cold end to the hot end (Fig. 3). The temperature

Table 1 Rocket engine design parameters

Parameter description	Design value
Cylinder radius	300 cm
Cylinder length	1000 cm
Inlet pressure	217 atm
H_2 temperature-shield entrance	300 K
H_2 temperature-shield exit	3000 K
H_2 temperature-core	4200 K
Specific impulse	1630 s
Mass flow rate	1150 kg s^{-1}
Antiproton annihilation rate	890 μgm s^{-1}
Antiproton mass annihilated	0.3 gm
Maximum temperature-tungsten	3000 K
Maximum temperature-zirconia	2700 K
Thrust/weight	4.75

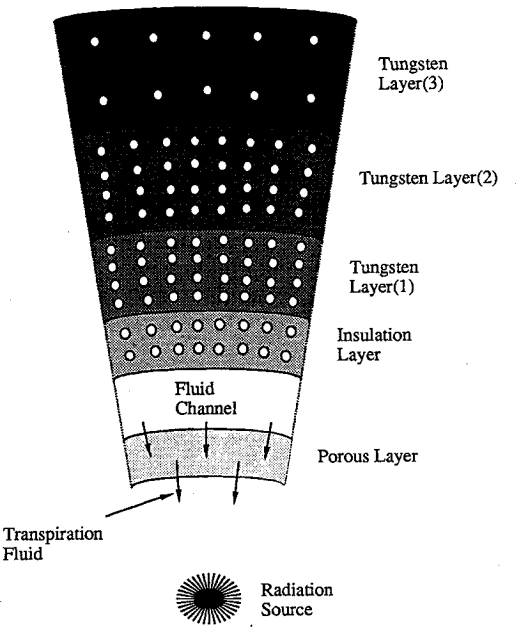

Fig. 2 Axial cross section of shield wall.

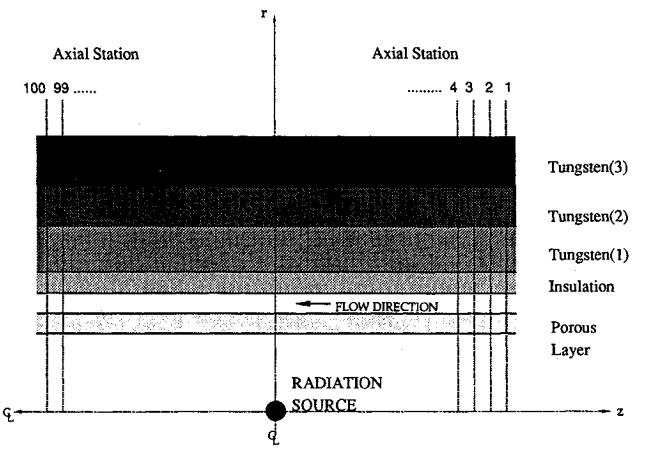

Fig. 3 Longitudinal shield geometry.

profile is calculated at each station starting at the cold end (aft end) and proceeding toward the hot end. The properties of the hydrogen fluid are updated at each location and are used at the next station to calculate the temperature profile there. For the porous layer, an exact solution is used. This is made possible by calculating an average power density that is constant in this layer. This average is computed by numerically integrating the expression for the power deposition by radiation over the volume element at each axial station. Finite difference equations are used in the insulation and

Table 2 Optimization results for three-shell model

Design variable	Parameter description	Initial	Optimized
X_1	Antiproton annihilation rate	125 μgm s^{-1}	534
X_2	Mass flow transpiration channel	198 kg s^{-1}	203
X_3	Mass flux porous layer	0.6 kg m^{-2} s^{-1}	0.89
X_4	Thickness-porous layer	2 cm	2.27
X_5	Thickness-transpiration channel	2 cm	2.30
X_6	Thickness-insulation	2.5 cm	2.94
X_7	Thickness-tungsten layer (1)	3 cm	4.60
X_8	Thickness-tungsten layer (2)	3 cm	2.90
	Thickness-tungsten layer (3)	cm	9.3
X_9	Tube density-insulation	3.214 tubes cm^{-2}	3.00
X_{10}	Tube density-tungsten (1)	3.214 tubes cm^{-2}	2.88
X_{11}	Tube density-tungsten (2)	3.214 tubes cm^{-2}	3.00
X_{12}	Tube density-tungsten (3)	0.25 tubes cm^{-2}	0.23
X_{13}	Density factor-tungsten (1)	0.4	0.23
X_{14}	Density factor-tungsten (2)	0.9	0.75
X_{15}	Tube diameter	4.75	5.16
	Fluid bulk temperature		2,219 K
	Tungsten maximum temperature		2,801 K
	Porous layer maximum temperature		2,700 K
	Insulation maximum temperature		2,692 K
	Specific impulse		1,037 s
	Mass of shield as optimized		400,000 kg
	Mass flow through engine		1,150 kg s^{-1}
	Maximum pressure drop		30 atm

tungsten layers. Three models were developed: 1) two-shell, 2) three-shell, and 3) four-shell. These models contain 2, 3, and 4 layers of tungsten after the insulation layer. More layers allows the power density to be spread through more of the shield and improves the performance. The density is varied in the different layers of tungsten by allowing each layer to have a different density of cooling tubes and a density factor that decreases the density from that of pure tungsten. Because the thermal conductivity is different in the insulation and in the different layers of the tungsten portion of the shield, each layer of the shield is differenced separately. The source terms required by the difference equations are computed from the expression for the power deposition by radiation. Heat removal is provided by tubes running through the shield with the hydrogen working fluid as a coolant. Instead of modeling the detailed heat transfer of the actual tube geometry, a "sink" term is computed at each location required by the difference equations. This sink term is based on the local density of tubes measured by the number of tubes per unit cross-sectional area of the structure and the temperature difference between the fluid and the shield at that point. Details of the analysis can be found in Refs. 11 and 12.

In Table 2 the design variables for a candidate optimized engine are shown. The output bulk temperature from the shield is 2219 K and the amount of antimatter annihilated was 534 μgm s^{-1}. From data supplied by Callas,[13] it is known that 26.7% of the annihilation energy will heat the working fluid above the 2219 K shield exit temperature. Using estimates of hydrogen specific heats, the bulk temperature in the core is 3370 K and the I_{sp} is 1037 s. This compares favorably with nuclear engines tested in the Rover/NERVA program[14] with specific impulses from 775–845 s. It does not, however, reach the design goal of 1630 s.

A surface plot of the structural temperature profile is shown in Fig. 5. This profile is for the structure starting at the inner boundary at 300 cm and working outward to the outer edge. The profile is symmetric in the azimuthal direction. The foreground is the cold end and the hot end is towards the back of the figure. As expected, heat is conducted axially by the fluid so the temperature rises from the cold end to the hot end, and because the heat source from radiation is attenuated in the inner regions of the shield, the outer section of the shield is relatively cold. The sharp drop in temperature across the porous layer can be seen in Fig. 5 and is due to the

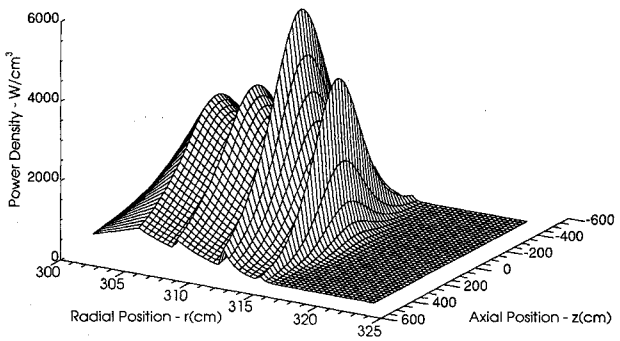

Fig. 4 Power density profile.

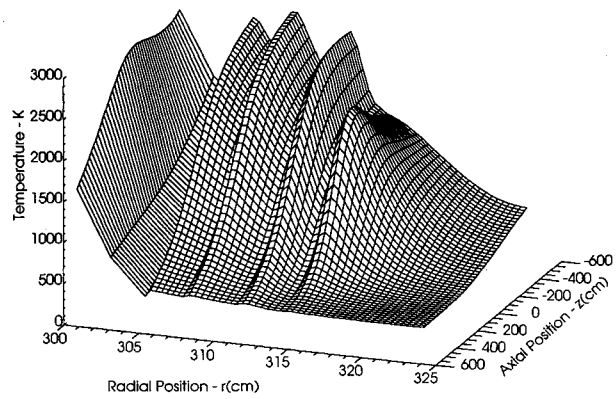

Fig. 5 Shield temperature profile.

effectiveness of the transpiration cooling. The peaks and valleys in the temperature profile in the tungsten layer can best be understood by looking at Fig. 4, which is a profile of the power density that is deposited in the shell by the annihilation radiation. The profile is symmetric about the middle of the cylindrical engine and exhibits the dying exponential behavior expected of radiation attenuation. The spikes are caused by the abrupt increases in density in the different layers of the tungsten shield. The power density in the porous and insulation layers is much smaller because of the reduced density of those materials. These peaks would be much more rounded if a more realistic analysis of the heat transfer using the actual

geometry of tube placement in the various layers were to be performed.

Optimization

The design optimization problem is cast into nonlinear mathematical programming form, and is solved using the method of feasible directions as implemented in the software package CONMIN.[15] The objective function to be minimized, $f(\boldsymbol{X})$, is subject to a number of inequality constraints $\boldsymbol{g}(\boldsymbol{X}) \leq 0$, where $\boldsymbol{X}$ is a vector of design variables.

The objective function for this problem is the total bulk temperature T_{bulk} of the hydrogen fluid at the exit of the tungsten shield. Since the desire is to maximize this temperature, it is recast as a minimization problem and scaled by a reference value of 3000 K as

$$f(\boldsymbol{X}) = -(T_{\text{bulk}}/3000\ \text{K}) \tag{1}$$

The total bulk temperature was computed by a simple mass average from

$$T_{\text{bulk}} = \frac{1}{\sum \dot{m}} \left(\sum_{i=1}^{n} T_{\text{bulk},i} \dot{m}_i + \sum_{j=1}^{100} T_{\text{porous},j} \dot{m}_j \right) \tag{2}$$

where i indexes the mass flow from the shield at radial locations, and j indexes the mass flow from the porous layer at the axial locations.

The design variables for the three-shell model are listed in Table 2. The antiproton annihilation rate (design variable 1) controls the energy input to the system. The annihilation rate is assumed to be equal to the rate of injection of antimatter into the combustion chamber. The mass flow in the transpiration channel (2) is the fluid flowing behind the porous layer that supplies the mass flux to the porous layer (3). Design variables 4–8 are the thicknesses of the various layers in the shield, and variables 9 through 12 are the tube densities in the insulation and tungsten layers. To allow a further variation in the density of the tungsten layers, a density factor (13, 14) is included for the tungsten layers 1 and 2. The outermost layer of tungsten does not have a density factor. The last variable (15) is the diameter of the tubes carrying the cooling fluid through the shield.

For the two-shell model, design variables 8, 12, and 14 were removed because there are only two layers of tungsten after the insulation layer. For the four-shell model, 3 variables (tungsten layer 3 thickness, tube density in tungsten layer 3, and density factor in tungsten layer 3) were added because an extra layer of tungsten is added.

There are 21 behavior constraints in the three-shell model. The tungsten temperature is constrained to be less than $T^{\max}_{\text{tungsten}} = 3000$ K in each of the tungsten layers, and the temperature in the insulation and the porous layer was constrained to be less than $T^{\max}_{\text{zirconia}} = 2700$ K. There is a pressure drop constraint on the fluid flowing in each of the shield layers. There is a constraint to prevent the mass flow through the porous layer from being greater than the mass flowing in the transpiration channel. There is an upper bound on the mass flux through the porous layer. This comes from the work of Green[16] that showed a minimum pressure drop for a mass flux of 0.9 kg m^2 s^{-1}, albeit at a lower pressure of 20 atm. Side constraints are placed on the thicknesses of the porous layer and the transpiration channel thickness to prevent them from becoming zero. There are upper bounds on the density of tubes in each layer that depend on the tube diameter and a factor k, that depends on the tube packing geometry. A simple geometry with adjacent rows of tubes shifted by half the tube center-to-center distance was chosen. The wall thickness was chosen so that all wall thicknesses were equal. This yields a factor of $k = 0.803519$. There are upper bounds on the density factors in the tungsten layers to prevent them from being heavier than the actual density, and there is a constraint that prevents the tube density in the outer tungsten layer from being less than zero.

These constraints were formulated as

Material temperature constraints:

$$g_1 = \frac{T^{\max}_{\text{porous}}}{T^{\max}_{\text{zirconia}}} - 1 \tag{3}$$

$$g_2 = \frac{T^{\max}_{\text{insulation}}}{T^{\max}_{\text{zirconia}}} - 1 \tag{4}$$

$$g_3 = \frac{T^{\max}_{\text{tungsten}}}{T^{\max}_{\text{tungsten}}} - 1 \tag{5}$$

$$g_4 = \frac{T^{\max}_{\text{tungsten2}}}{T^{\max}_{\text{tungsten}}} - 1 \tag{6}$$

$$g_5 = \frac{T^{\max}_{\text{tungsten2}}}{T^{\max}_{\text{tungsten}}} - 1 \tag{7}$$

Pressure drop constraints:

$$g_6 = \frac{\Delta P^{\max}_{\text{transpiration}}}{\Delta P^{\max}} - 1 \tag{8}$$

$$g_7 = \frac{\Delta P^{\max}_{\text{insulation}}}{\Delta P^{\max}} - 1 \tag{9}$$

$$g_8 = \frac{\Delta P^{\max}_{\text{tungsten1}}}{\Delta P^{\max}} - 1 \tag{10}$$

$$g_9 = \frac{\Delta P^{\max}_{\text{tungsten2}}}{\Delta P^{\max}} - 1 \tag{11}$$

$$g_{10} = \frac{\Delta P^{\max}_{\text{tungsten3}}}{\Delta P^{\max}} - 1 \tag{12}$$

Transpiration mass flow upper bound:

$$g_{11} = \frac{\dot{m}_{\text{porous}} + 20\ \text{kg s}^{-1} - X_2}{20} \tag{13}$$

Porous layer mass flux upper bound:

$$g_{12} = X_3 - 0.9\ \text{kg m}^{-2}\ \text{s}^{-1} \tag{14}$$

Porous layer thickness lower bound:

$$g_{13} = -X_4 + 1\ \text{cm} \tag{15}$$

Transpiration channel thickness lower bound:

$$g_{14} = -X_5 + 1\ \text{cm} \tag{16}$$

Tube density upper bounds:

$$g_{15} = X_9 - [k/(X_{15})^2] \tag{17}$$

$$g_{16} = X_{10} - [k/(X_{15})^2] \tag{18}$$

$$g_{17} = X_{11} - [k/(X_{15})^2] \tag{19}$$

$$g_{18} = X_{12} - [k/(X_{15})^2] \tag{20}$$

Density factor upper bounds:

$$g_{19} = X_{13} - 1 \tag{21}$$

$$g_{20} = X_{14} - 1 \tag{22}$$

Tube density in tungsten layer 3 lower bound:

$$g_{21} = -X_{12} \tag{23}$$

For the two-shell model, constraints associated with the third layer were removed, and for the four-shell model, constraints associated with the fourth layer were added.

The solution process was by direct connection of the analysis to CONMIN that calculated all gradient information using finite difference approximations. The iteration histories of the scaled variables and active constraints for the three-shell optimization run shown in Table 2 are displayed in Figs. 6–13. This three-shell model was run with a maximum allowed pressure drop of 30 atm. This was chosen as the baseline pressure

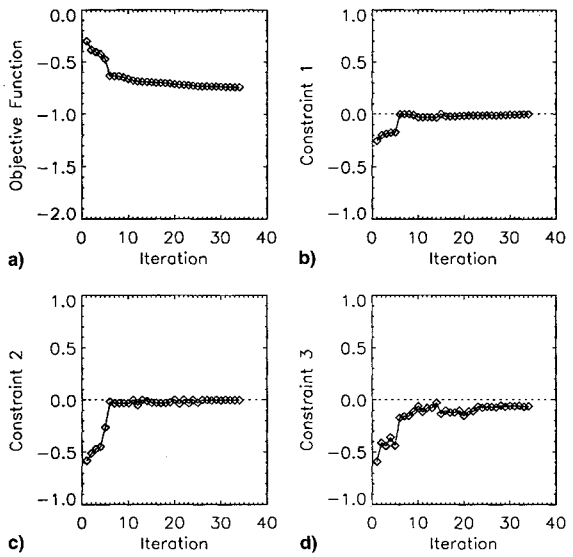

Fig. 6 Objective function and constraints 1–3: a) fluid bulk temperature, b) porous temperature, c) insulation temperature, and d) tungsten layer 1 temperature.

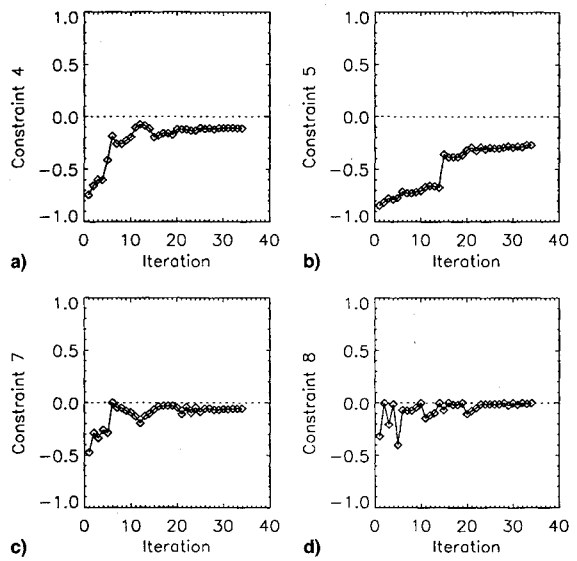

Fig. 7 Constraints 4, 5, 7, and 8: a) tungsten layer 2 temperature, b) tungsten layer 3 temperature, c) insulation pressure, and d) tungsten layer 1 pressure.

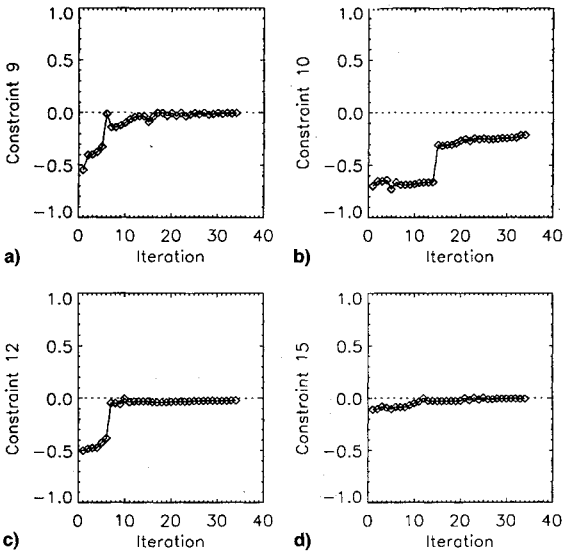

Fig. 8 Constraints 9, 10, 12, and 15: a) tungsten layer 2 pressure, b) tungsten layer 3 pressure, c) porous mass flux, and d) insulation tube density.

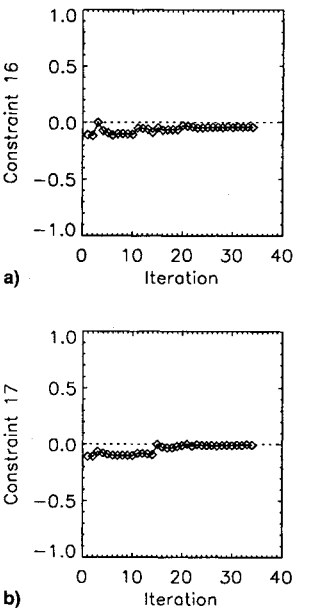

Fig. 9 Constraints 16 and 17: a) tungsten layer 1 tube density and b) tungsten layer 2 tube density.

drop because it is similar (as a percent of inlet pressure) to the pressure drops in nuclear thermal engines. The convergence criterion was that the relative change in the objective function for 3 successive iterations was less than 0.001 after 33 iterations on a Sun Sparc 2 processor that used 11.7 cpu h. The objective function was evaluated 580 times. At the end point, constraints 1, 2, 8, 9, and 15 were active with a constraint thickness of -0.004. The constraints that were active during the optimization were constraints 1, 2, 3, 7, 8, 9, 12, 15, 16, and 17. Additional runs were done to check the sensitivity of the optimum to the starting point. If a run was started in the same general vicinity, the run ended at slightly different design points, but gave a similar (within 5%) bulk temperature. This behavior suggests that the design space is essentially convex and is rather "flat" in the vicinity of the optimum.

Using the three-shell model, grid independence was checked. An optimization was done using a grid that contained 30 points radially through the insulation and tungsten, and 100 points axially. The radial grid density was doubled to 60 points,

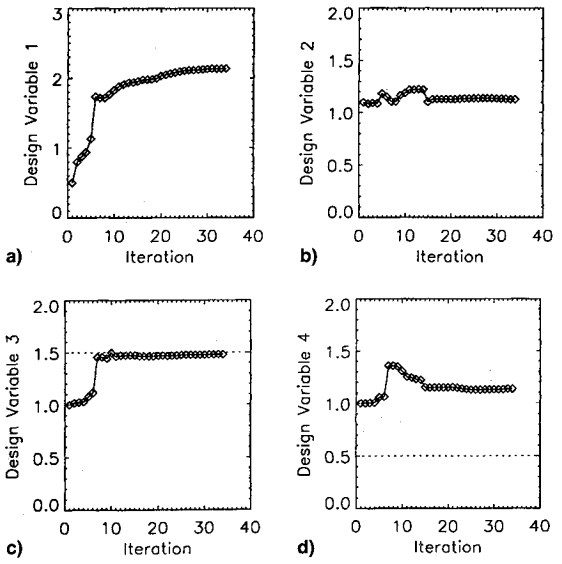

Fig. 10 Design variables 1–4: a) P-bar rate, b) transpiration mass flow, c) porous layer mass flux, and d) porous layer thickness.

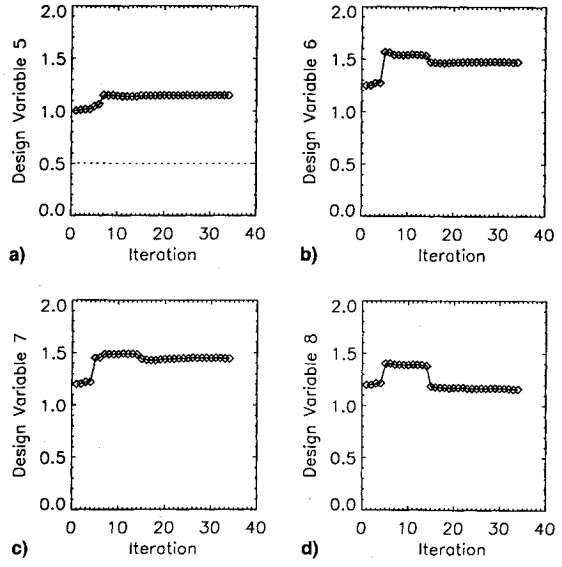

Fig. 11 Design variables 5–8: a) transpiration channel thickness, b) insulation thickness, c) tungsten layer 1 thickness, and d) tungsten layer 2 thickness.

and the optimization rerun. The bulk temperature was 3% lower and the resulting design variables were only slightly different. This difference is attributed to the fact that with a denser grid the peak temperatures are elevated, and so the constraints become active at different points in the optimization.

A run of the three-shell model was done with the upper bound constraint on the porous layer mass flux removed. The bulk temperature was within 2% of the bulk temperature with the porous layer mass flux bounded. The mass flux increased to 1.56 kg m^{-2} s^{-1}, and there were large differences in other design variables. While this mass flux may not be unreasonable, the upper bound was left in for the balance of the optimization runs.

The performance of two-, three-, and four-shell models are compared in Fig. 14. As can be seen, the addition of shells allows the attenuation of radiation to be controlled for a performance gain. The densities of the shells can be tailored to improve the output bulk temperature. However, the performance improvement associated with the addition of a layer is less than 10%.

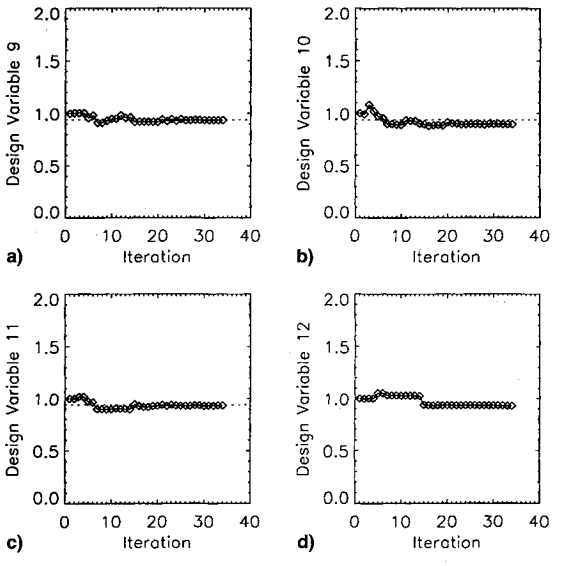

Fig. 12 Design variables 9–12: a) insulation tube density, b) tungsten layer 1 tube density, c) tungsten layer 2 tube density, and d) tungsten layer 3 tube density.

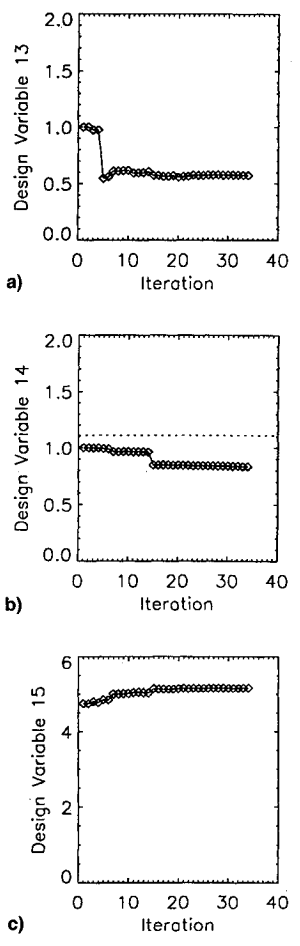

Fig. 13 Design variables 13–15: a) tungsten layer 1 density factor, b) tungsten layer 2 density factor, and c) cooling tube diameter.

Additional runs of the three-shell model with different allowed pressure drops were done and are compared in Fig. 15. As expected, allowing greater pressure drops increased the output bulk temperature. This improvement however, requires that the structure be able to withstand greater stresses caused by the pressure drop, and there is a decrease in I_{sp} from the lower combustion chamber pressure, which may be important when operating in the atmosphere.

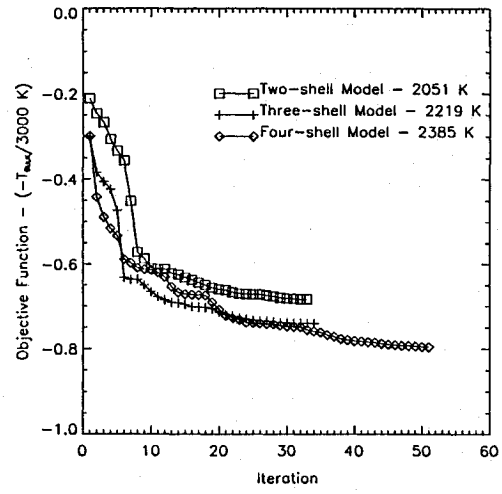

Fig. 14 Comparison of bulk temperature for 2-, 3-, and 4-shell models. Temperatures listed are final bulk temperatures.

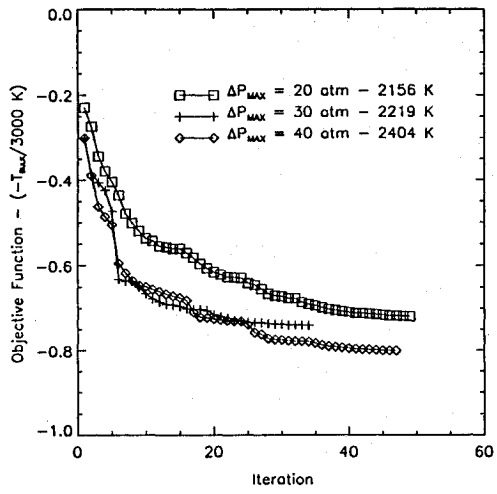

Fig. 15 Comparison of bulk temperatures with 20, 30, and 40 atm of pressure drop. Temperatures listed are final bulk temperatures for the 3-shell model.

Discussion

With respect to the three-shell model with an allowed pressure drop of 30 atm, the constraint imposed by the material temperature limits can be seen in that the temperature constraint on zirconia was active in both the porous and insulation layers at the optimum. The temperature constraint on tungsten in layer 1 was active during the run, but not at the optimum. The constraint on pressure drop is also very important. At the optimum, the pressure drop constraints in tungsten layers 1 and 2 were active, and the pressure drop constraint in the insulation layer was active during the optimization run. In the run in which the pressure drop constraint was relaxed to 40 atm, the active constraints at the optimum were constraints 3 and 5, which are tungsten temperature constraints. There is a tradeoff between pressure drop and increased performance that merits further study, but will require the inclusion of an analysis of the structural problem.

For the baseline case, the other active constraint at the optimum was constraint 15, the upper bound on tube density in the insulation layer. Additionally, the upper bounds on tube densities in tungsten layers 1 and 2 were active during the run. Since the tube geometry packing factor was not a design variable in this optimization, it merits further investigation. A more detailed analysis of wall thickness and packing geometry could be included with the potential for improved performance.

The upper bound on the porous layer mass flux was active during the optimization, but not at the optimum. As noted, when this upper bound is deleted the mass flux increases substantially, but the improvement in performance is small. The design of the porous layer will be dictated by structural concerns and a more detailed analysis needs to be done.

Conclusions

A code has been developed that can be used to evaluate the performance limit of high-energy rocket engine designs. This code, if coupled with an appropriate neutronics code, could be used to evaluate nuclear thermal rocket designs. A point design test case was evaluated using this procedure, and the performance constraints identified. Several areas were identified for further research that could improve this design. The optimization problem, as formulated in the present study, appears to be well behaved. No local minima were encountered, and convergence was easily reached.

Acknowledgments

The authors would like to acknowledge the following people for their contributions to this article: Robert Forward for his comments that initiated this investigation on gas-core engines; John Callas at JPL for his time and effort in running his Monte-Carlo code to provide numbers for engine efficiencies; David Peaslee in the University of Maryland Department of Physics and Astronomy for discussions about the particle physics involved; and Roberto Celi in the University of Maryland Department of Aerospace Engineering for his assistance with the optimization work.

References

[1]Sänger, E., "Zur Theorie der Photonenraketen," *Ingenieur-Archiv*, Vol. 21, 1953, pp. 213–226.

[2]Forward, R. L., *Antimatter Annihilation Propulsion*, AFRPLTR-85-034, Sept. 1985.

[3]Vulpetti, G., et al., "Simultaneous Optimization of Payload Mass and Antimatter Energy for a Fully-Reusable Single-Stage-to-Orbit Launch Vehicle," 38th Congress of the International Astronautical Federation, Preprint IAF-87-330, Brighton, England, UK, Oct. 1987.

[4]Borowski, S. K., "A Comparison of Fusion/Antiproton Propulsion Systems for Interplanetary Travel," AIAA Paper 87-1814, June 1987.

[5]Cassenti, B. N., "Design Considerations for Relativistic Antimatter Rockets," *Journal of the British Interplanetary Society*, Vol. 35, 1982, pp. 396–404.

[6]Howe, S. D., and Metzger, J. D., "Antiproton-Based Propulsion Concepts and the Potential Impact on a Manned Mars Mission," *Journal of Propulsion and Power*, Vol. 5, No. 3, 1989, pp. 295–300.

[7]LaPointe, M. R., "Antiproton Powered Propulsion with Magnetically Confined Plasma Engines," AIAA Paper 89-2334, July 1989.

[8]Peaslee, D. C., "Potential Low Energy P-Bar Sources in the U.S.," *Proceedings of the RAND Workshop on Antiproton Science and Technology* (Santa Monica, CA), World Scientific Publishing, Teaneck, NJ, 1988.

[9]Gabrielse, G., et al., "Cooling and Slowing of Trapped Antiprotons Below 100 Mev," *Physical Review Letters*, Vol. 63, No. 13, 1989, pp. 1360–1363.

[10]Tarpley, C., and Lewis, M. J., "Radiation Safety Issues in Single-Stage-To-Orbit Spacecraft Powered by Antimatter Rocket Engines," *Journal of Propulsion and Power*, Vol. 8, No. 1, 1992, pp. 127–135.

[11]Tarpley, C., and Lewis, M. J., "Optimized Design of an Antimatter Booster Rocket," AIAA Paper 91-1923, July 1991.

[12]Tarpley, C., "The Design and Optimization of a Shielded Gas-Core Antimatter Rocket Engine," M.S. Thesis, Univ. of Maryland, College Park, MD, 1991.

[13]Callas, J. L., private communication, Jet Propulsion Lab., Jan.–May 1990.

[14]Sievers, R., Livingston, J., and Pierce, B., "NERVA Propulsion System Design Considerations," AIAA Paper 90-1951, July 1990.

[15]Vanderplaats, G. N., and Moses, F., "Structural Optimization by Methods of Feasible Directions," *Computers and Structures*, Vol. 3, 1973, pp. 739–755.

[16]Green, L., Jr., "Gas Cooling of a Porous Heat Source," *Journal of Applied Mechanics*, Vol. 19, No. 2, 1952, pp. 173–178.